ACS APPLIED MATERIALS & INTERFACES

www.acsami.org

Research Article

A Smart Finger for Soft Material Identification Based on a Multimodal Tactile Sensor

Lu Wang,[§] Puchuan Tan,*[,§] Xuecheng Qu,[§] Shengyu Chao, Yuan Xi, Yang Zou, Cong Li, Jiangtao Xue, and Zhou Li*

Cite This: https://doi.org/10.1021/acsami.5c17508

Read Online

ACCESS | Metrics & More | Article Recommendations | Supporting Information

ABSTRACT: Existing artificial tactile sensing technologies face significant challenges in addressing signal instability caused by the complex mechanical responses of soft materials. Here, a multimodal smart tactile finger based on a triboelectric nanogenerator (TENG) and a piezoelectric nanogenerator (PENG) is developed. The smart finger system integrates a stable contact mechanism with a multimodal sensing module, enabling the synchronous acquisition of composite responses from four TENG channels and one PENG channel. For different soft materials, the TENG and PENG signals generated during the detection process are significantly different. The former is generated by the contact and separation of the TENG module and the soft materials, while the latter is generated by the elastic collision between the PENG module and the soft materials. The acquired signals are standardized and processed using a linear discriminant analysis (LDA) model to achieve accurate classification of soft material types. Testing with 23 soft materials covering broad ranges of modulus and adhesion strength demonstrates that the classification accuracy with all five channels exceeds 83%, significantly outperforming results from any single sensor channel. This smart tactile finger offers promising technological prospects for advanced human−machine interaction, bioinspired robotics, and medical tactile systems.

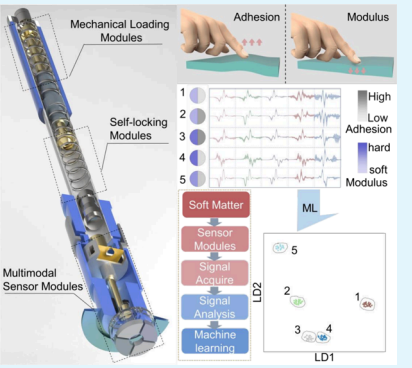

KEYWORDS: *tactile sensor, triboelectric nanogenerator, piezoelectric nanogenerator, material identification, machine learning*

1. INTRODUCTION

Tactile perception is the primary means by which humans perceive the mechanical and geometric properties of an object's surfaces, and its function relies on the response of cutaneous mechanoreceptors in the skin to external physical stimuli such as pressure, shear, vibration, and temperature.[1] Artificial tactile sensing aims to emulate this perceptual process,[2,3] however, due to the absence of diverse mechanoreceptors and corresponding neural processing mechanisms found in biological skin,[4] it still faces significant challenges in accurately replicating human tactile experiences,[5] particularly in the perception of objects with complex mechanical properties.[6] Soft materials generally refer to materials characterized by low modulus and significant deformability,[7] such as hydrogels,[8] polymers,[9] and biological tissues.[10] These materials are prevalent in polymeric composites and flexible electronic systems, demonstrating extensive potential in healthcare and materials processing fields.[11] The mechanical properties of soft materials directly influence their functional suitability.[12] Rapid and accurate identification of soft material types is of great significance for applications such as material sorting, flexible robot interaction, and bionic sensing.[13]

Currently, the characterization of soft materials' mechanical properties, including modulus and adhesion strength, predominantly depends on laboratory instruments such as atomic force microscopy,[14] indentation testing,[15] tensile testing, thermal conductivity,[16] ultrasound,[17] computer vision,[18,19] etc.[20−25] Although these methods accurately provide material parameters such as modulus and adhesion strength, limitations including high equipment costs, complicated operations, and low measurement efficiency restrict their suitability for rapid in *situ* or field testing. Therefore, there is an urgent need to develop identification techniques that are cost-effective, efficient, and easily integrated (see Table S1 for comparison with previous studies).

TENG and PENG have received widespread attention in self-powered sensing technologies due to their inherent advantages of requiring no external power supply and being readily integrable.[26−31]

The working principle of TENG relies on the triboelectric effect,[32,33] which originates from the charge transfer at the interface of two contacting materials and generates an electrical signal that is highly sensitive to the microscopic physical

Received: September 3, 2025
Revised: November 27, 2025
Accepted: November 28, 2025

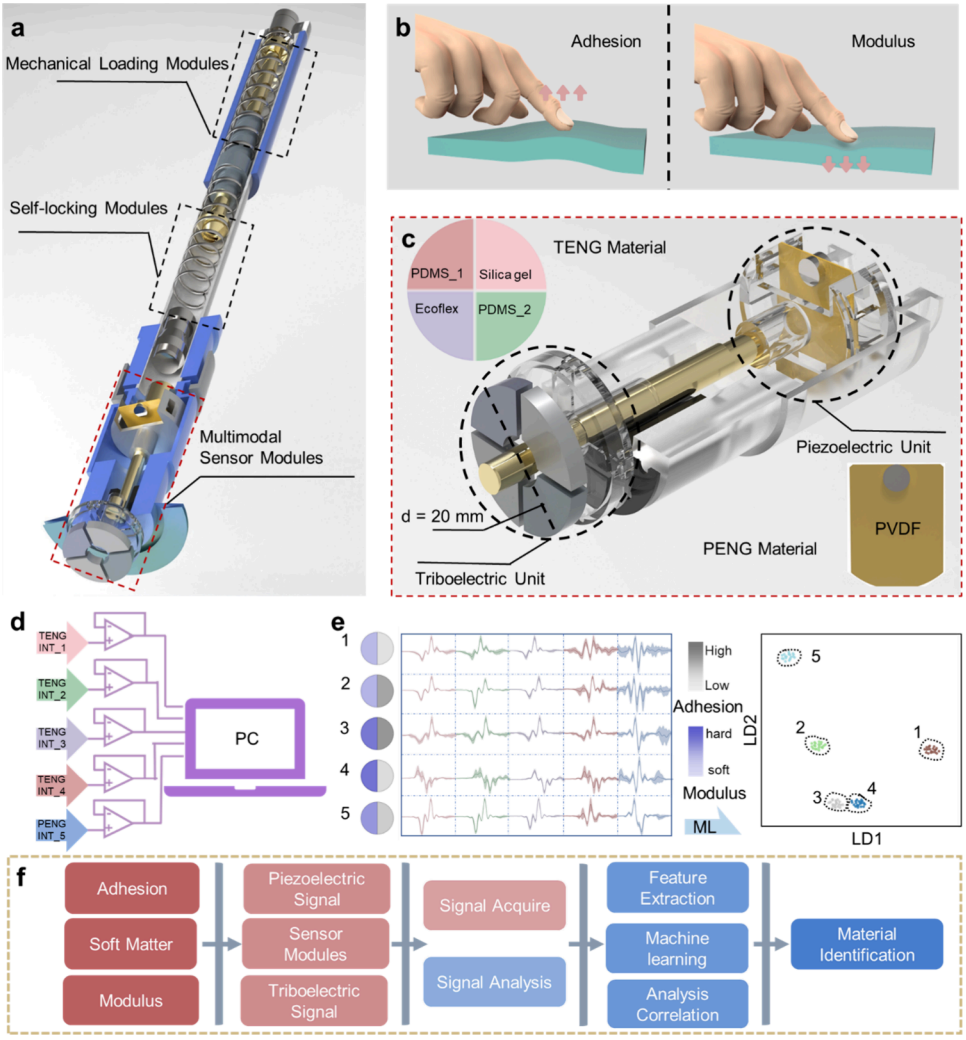

Figure 1. Schematic illustration of the smart finger system and its working principles. (r) Cross-sectional view of the device. (b) Schematic of material identification. (c) Enlarged view of the sensing module. (d) Signal acquisition and transmission process. (e) Representative sample testing results with averaged waveforms. (f) Workflow diagram illustrating the interaction between system modules for identification.

properties of the contacting surface.[34] Prior studies have demonstrated artificial tactile fingers based on triboelectric sensing,[35−37] capable of identifying a wide range of solid material surfaces, achieving average classification accuracies of approximately 97%. In soft material systems, variations in electron affinity, modulus,[38] surface texture,[39] and adhesion strength result in distinct contact−separation process and charge transfer behaviors,[40−43] thereby leading to triboelectric signals with strong material dependence. Based on this principle, TENG sensor array composed of materials with different modulus and adhesion strength can be constructed to effectively classify soft materials by analyzing their distinct electrical responses.[44,45]

The working principle of PENG is based on the piezoelectric effect, which refers to the generation of electric potential in a material due to lattice polarization under the application of mechanical stress.[46−48] In particular, cantilever beam structures utilizing piezoelectric materials, such as polyvinylidene fluoride (PVDF), can convert minute deformations at the free end into detectable electrical signals with high sensitivity.[49,50] When the cantilever beam structure collides with the soft material, the modulus of the soft material determines the degree of deformation and energy absorption, thereby adjusting the dynamic response of the PVDF cantilever beam. Therefore, the piezoelectric signal serves as an effective indicator of the material's modulus.[51]

Based on the aforementioned sensing mechanisms, this work proposes a multimodal smart finger (MSF) system for the identification of soft materials. The system adopts an integrated structural design that incorporates a mechanically stable loading mechanism and a multimodal sensing module, ensuring consistent mechanical contact conditions while enabling simultaneous acquisition of triboelectric and piezoelectric signals. Machine learning-based data processing enhances classification accuracy,[52−54] allowing the system to discriminate soft materials based on adhesion properties and internal elastic responses. This study not only demonstrates the synergistic roles of TENG and PENG in mechanical characterization of soft materials, but also presents a scalable, low-power, and high-throughput tactile identification strategy. The proposed system establishes a technological foundation for rapid classification and condition monitoring of soft materials in applications such as intelligent prosthetics, flexible robotic perception, and human−machine interface systems.

https://doi.org/10.1021/acsami.5c17508
ACS Appl. Mater. Interfaces XXXX, XXX, XXX−XXX

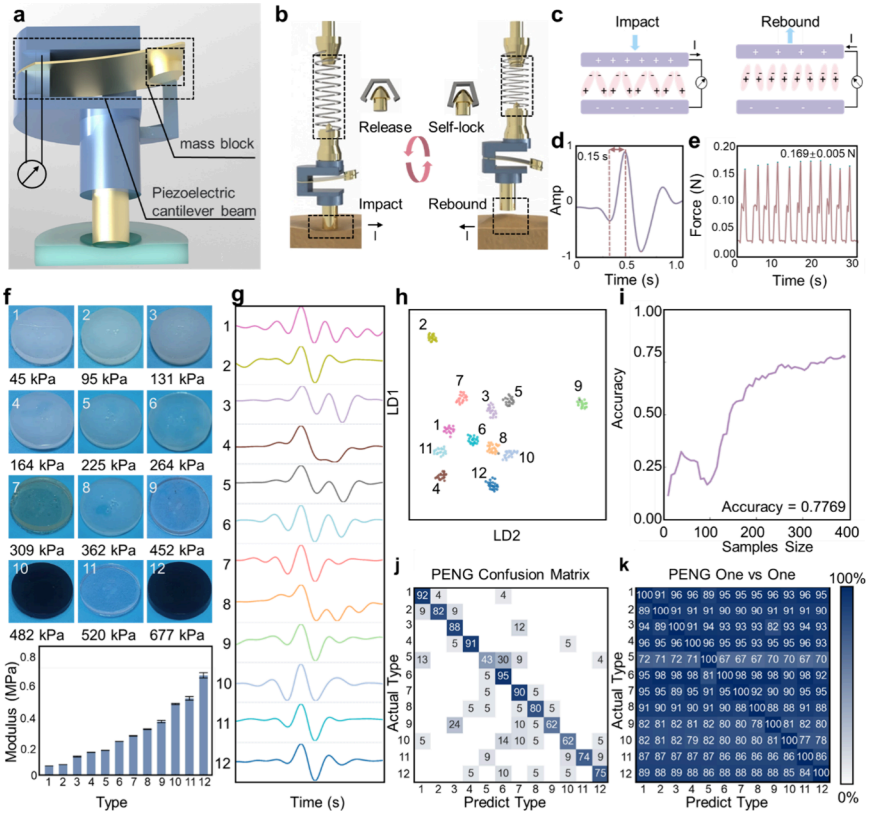

Figure 2. Structure and working principle of the PENG modules and identification performance for samples with different moduli. (a) Schematic of the PENG modules. (b) Diagram of the impact−lock−release process. (c) Working principle of the piezoelectric effect. (d) Piezoelectric signal waveform under a single impact. (e) Reproducibility test of instantaneous impact force during loading−impact-rebound events. (f) Photographs and modulus distribution of 12 soft material samples. (g) Averaged piezoelectric waveforms under repeated impact responses. (h) Sample clustering results in the two-dimensional discriminant feature space. (i) Evolution of validation accuracy with increasing training samples. (j) Confusion matrix. (k) One-vs-one classification matrix.

2. RESULTS

2.1. Design and Integration of the MSF. This study presents a pen-shaped MSF based on TENG and PENG, with an overall size of approximately 190 mm × 20 mm and a total weight of about 72 g, offering good portability and stable hand-held operation (Figure 1a). The MSF integrates a mechanical loading module, a self-locking module, and a multimodal sensor module.

During soft material identification, The suction cup at the tip of the MSF is first aligned and pressed against the surface of the target sample. Manual downward force is applied until the self-locking mechanism is engaged, ensuring stable contact between the TENG sensor array and the sample. Upon release of the locking structure, the precompressed spring is triggered to discharge stored mechanical energy, driving the impact head to deliver a standardized impulse to the sample and eliciting a dynamic response from the PENG module. This integrated structure allows the simultaneous acquisition of triboelectric and piezoelectric signals in a single actuation, enabling comprehensive sensing of both adhesion properties and internal mechanical characteristics (Figure 1b).

The sensor module integrates two mechanisms: a TENG sensor array composed of four soft materials with modulus and adhesion properties, which respond to contact−separation process at the interface, and a piezoelectric module based on a PVDF cantilever beam, which responds to transient elastic deformation under impact loading (Figure 1c). These signals respectively reflect modulus and adhesion characteristics of the material, providing integrated information to enhance the discriminability of soft material mechanical characterization.

The sensing signals are routed to the microcontroller unit via a multichannel interface, enabling synchronous acquisition and preliminary processing. These data are then transmitted to a host computer through wired communication (Figure 1d).

To visually demonstrate the device's ability to distinguish representative samples, Figure 1e presents results from five materials with distinct combinations of modulus and adhesion strength. In the resulting low-dimensional feature space, these materials form clearly separated clusters. The two-dimensional visualization in this context was achieved using the Uniform Manifold Approximation and Projection (UMAP) algorithm solely for illustrative purposes, and the actual classification model is constructed entirely based on high-dimensional LDA analysis.

The overall workflow of the system is illustrated in Figure 1f. First, the adhesion and modulus of the target material jointly influence the responses of the triboelectric and piezoelectric sensing modules, generating distinctive multimodal signals. These signals are subsequently subjected to feature extraction, correlation analysis, and machine learning processing, ultimately enabling automatic identification of different materials.

2.2. Design and Integration of the Piezoelectric Measurement Structure. The PENG sensor module employs a PVDF cantilever beam structure made of PVDF with one end fixed and the other free to allow sensitive

https://doi.org/10.1021/acsami.5c17508
ACS Appl. Mater. Interfaces XXXX, XXX, XXX−XXX

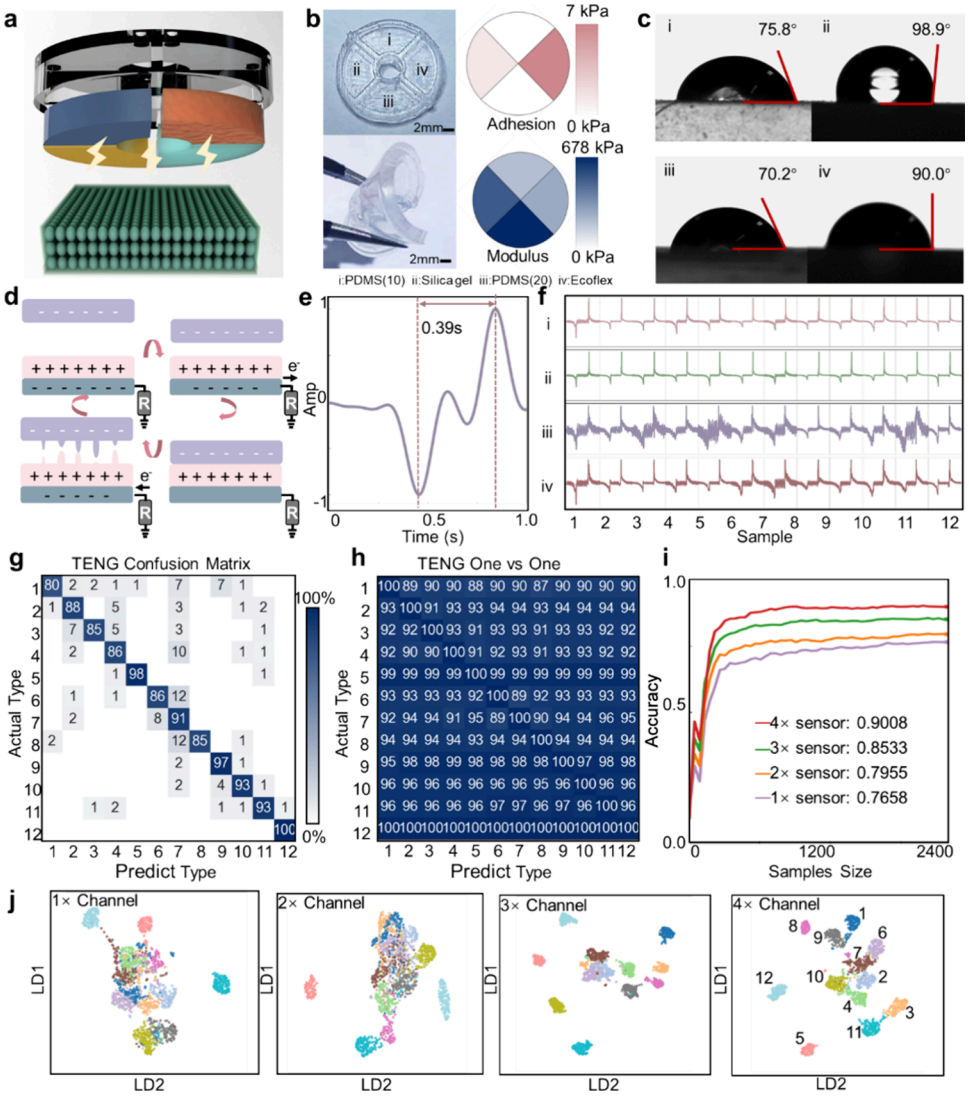

Figure 3. Structure and working principle of the TENG sensor array and identification performance for samples with different moduli. (a) Schematic diagram of the TENG sensor array. (b) Flexible substrate and four triboelectric layer materials with their mechanical property distributions. (c) Static contact angle measurements of the triboelectric layer materials. (d) Working principle of the TENG. (e) Response waveform of triboelectric signal during a single contact−separation cycle. (f) Representative signals generated during contact with 12 soft materials, synchronously sampled across four channels. (g) Confusion matrix of the LDA model trained using four-channel triboelectric signals. (h) One vs One classification probability matrix between each two material pairs. (i) Evolution of classification accuracy with training sample size under different sensor channel configurations. (j) Two-dimensional visualization of LDA output after UMAP dimensionality reduction, showing progressively improved class separability as the number of TENG sensor channels increases from 1 to 4.

dynamic response under external excitation (Figure 2a). One end of the PVDF film is firmly anchored to a rigid support structure to provide mechanical constraint, and its free end is loaded with a small mass to stabilize the vibration response. When subjected to external impact, the PVDF cantilever beam bends and vibrates, inducing charge transfer via the piezoelectric effect and converting mechanical deformation into an electrical output. To ensure consistent impact excitation, a manually preloaded spring mechanism is integrated into the module and equipped with a self-locking module (Figure 2b).

The signal generation mechanism of the PENG sensor module is illustrated in Figure 2c. Upon interaction between the impact head and the soft material (Figure S1), the PVDF cantilever beam undergoes bending vibrations. This mechanical deformation induces internal strain in the PVDF film, leading to a reorientation of dipole moments and the generation of a corresponding piezoelectric signal. The waveform characteristics of this signal are strongly correlated with the mechanical response of the impacted material, which is primarily determined by its modulus.

During experimental operation, the spring is first manually compressed to a preset level defined by the self-locking structure. Releasing the latch causes the stored elastic energy to be rapidly discharged, driving the impact head to deliver a transient mechanical impulse onto the surface of the target soft material. The impacted region experiences instantaneous local compression, followed by elastic recovery, with part of the energy being transferred back to the PVDF cantilever beam structure.

As shown in Figure 2d, after the release of the self-locking structure, the piezoelectric signal reaches its peak at approximately 0.15 s and decays to zero within several hundred milliseconds. Repeated impact tests confirm that the peak force applied to the material surface remains consistently

https://doi.org/10.1021/acsami.5c17508
ACS Appl. Mater. Interfaces XXXX, XXX, XXX−XXX

around 0.16 N with a fluctuation of only ± 0.005 N (Figure 2e), indicating that the self-locking module provides highly consistent and controllable impact excitation.

To validate the performance of the PENG sensor module, a total of 12 soft material samples with distinct moduli were selected for testing, yielding a range from approximately 45 to 677 kPa (Figure 2f). For each material class, no fewer than 40 independent impact measurements were performed using the PENG sensor module, and the corresponding dynamic response signals were collected (Figure 2g). The detailed number of tests for each material is summarized in Figure S10. These signals were subjected to feature extraction and classified by LDA model.

The classification results were visualized in two dimensions (Figure 2h), revealing clear boundaries between different material classes, indicative of distinct feature separability within the high-dimensional space. The data set was partitioned into a training set comprising 60% of the total samples and a validation set comprising the remaining 40%. As the training sample size increased, the classification accuracy on the validation set exhibited an overall upward trend (Figure 2i), achieving approximately 77.69% at around 400 training samples, suggesting the model's performance is relatively stable under sufficient training data.

The confusion matrix derived from the validation set (Figure 2j) shows that most classes achieved classification accuracies exceeding 70%. A few material classes with closely matched moduli (e.g., classes 5 and 6) exhibited moderate misclassification, highlighting areas of limited interclass resolution. Additionally, one-vs-one classification results (Figure 2k) further demonstrate the model's discriminative power, with most class pairs achieving accuracies above 80%, underscoring the model's robust one-vs-one classification capacity.

2.3. Design and Integration of the Triboelectric Sensing Structure. The TENG sensor array adopts an array composed of four soft materials with distinct mechanical characteristics, forming the functional layers of the sensor elements (Figure 3a).To accommodate the geometric deformation of soft samples, the compliant substrate was fabricated from flexible materials, while the outer layer adopted a suction cup architecture (Figure 1a) that provides stable elastic support, ensuring intimate surface conformity and a nearly constant contact area. In addition, a self-locking mechanism with tactile feedback (Figure 2b) was integrated to maintain a stable contact force during repeated triboelectric measurements. The triboelectric layers include two polydimethylsiloxane (PDMS) elastomers with different mixing ratios (10:1 and 20:1), a silicone gel, and Ecoflex rubber. These materials cover a broad spectrum of moduli and adhesion strength (Figure 3b), and exhibit markedly different hydrophilic properties (Figure 3c), thereby enhancing signal diversity and sensitivity in a single contact.

The sensor array operates in four single-electrode contact-separation mode TENGs, enabling simultaneous multichannel signal acquisition. During testing, each triboelectric layer undergoes periodic contact and separation with the target soft material. Owing to differences in electron affinity and interfacial interactions, contact electrification and electrostatic induction result in the generation of surface charges and corresponding voltage signals (Figure 3d). The signal characteristics are closely related to the physical properties of the contacted material, with surface modulus and adhesion strength playing prominent roles.

The sensor array operates in four single-electrode contact-separation mode TENGs, enabling simultaneous multichannel signal acquisition. During testing, each triboelectric layer undergoes periodic contact and separation with the target soft material. Owing to differences in electron affinity and interfacial interactions, contact electrification and electrostatic induction result in the generation of surface charges and corresponding voltage signals (Figure 3d). The signal characteristics are closely related to the physical properties of the contacted material, with surface modulus and adhesion strength playing prominent roles.

Given that variations in contact force and angle significantly affect measurement consistency (Figure S2), the MSF terminal is equipped with a fixture incorporating a suction cup to ensure stable contact (Figure S3). During testing, the TENG sensor array is manually pressed against the sample surface until the self-locking mechanism is triggered, ensuring uniform contact force. A representative voltage waveform from a single contact cycle is shown in Figure 3e, where the signal reaches its peak within approximately 0.39 s, demonstrating fast response suitable for downstream pattern identification.

To evaluate the sensor's performance, 12 soft materials with varying moduli were selected and tested under linear motor control (Figure 3f, Figure S4). For each material, no fewer than 200 independent contact measurements were performed (see Figure S10 for detailed sample numbers).In addition, the long-term durability of the triboelectric module was verified through cyclic fatigue testing, confirming stable signal output after nearly 2000 repeated operations (Figure S11). The influence of environmental factors such as temperature and humidity on the triboelectric performance was also examined, and the corresponding results are provided in the Supporting Information (Figures S15 and S16). Feature vectors were extracted from the triboelectric signals and used to construct a high-dimensional feature space. Classification was carried out using LDA and the model's performance is summarized in the confusion matrix (Figure 3g, Figure S5). Most materials were accurately classified, indicating that the sensor exhibits both high sensitivity and classification robustness in soft material identification tasks. Specifically, half material classes achieved classification accuracies above 90%, with the highest reaching 100% (class 12), and the lowest still maintaining over 80% (class 1), demonstrating a uniformly high classification quality.

Further analysis of one vs one classification probabilities (Figure 3h) confirms the high discriminative power of the TENG sensor array: the majority of material pairs achieved accuracies above 90%. A comparison of classification performance under different channel combinations (Figure 3i) highlights that increased channel count significantly enhances accuracy, with the four-channel setup yielding optimal results. The accuracy improved from 76.58% (single channel) to 90.08% (four channels), illustrating the clear advantage of

https://doi.org/10.1021/acsami.5c17508
ACS Appl. Mater. Interfaces XXXX, XXX, XXX−XXX

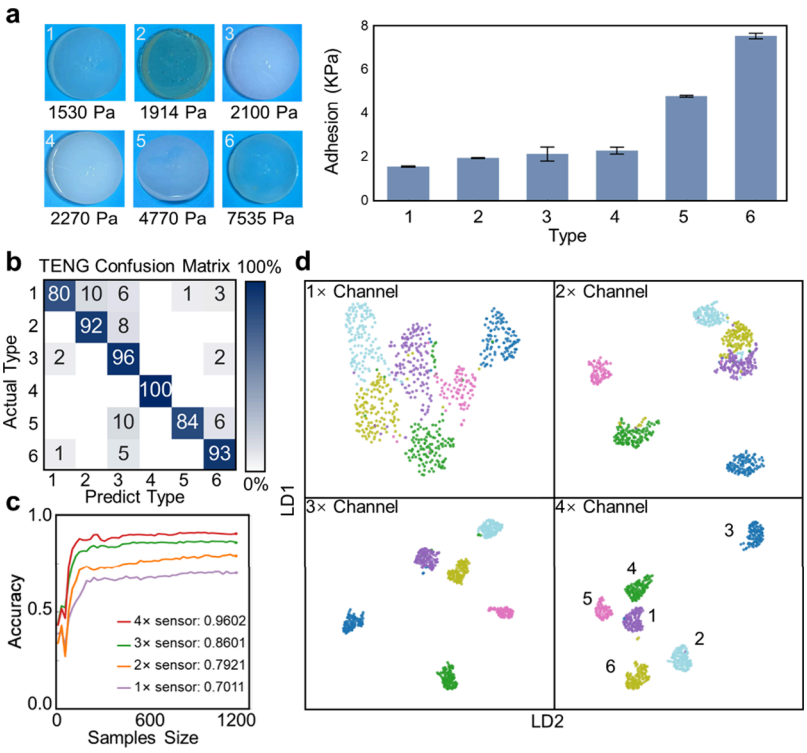

Figure 4. Identification performance for materials with different adhesion strength. (a) Photographs of six soft material samples and their adhesion strength distributions. (b) Confusion matrix of the LDA model trained using four-channel triboelectric signals. (c) Evolution of classification accuracy with training sample size under different sensor channel configurations. (d) Two-dimensional visualization of LDA output after UMAP dimensionality reduction, showing progressively improved class separability as the number of TENG sensor channels increases from 1 to 4.

multichannel data combination. To visualize the influence of channel number on class separability, we performed dimensionality reduction on the LDA feature space using a two-dimensional mapping (Figure 3j). From single to four-channel configurations, progressively clearer clustering boundaries emerged, with substantially reduced overlap between classes. This affirms the advantage of multichannel data combination in feature representation.

To further evaluate the capability of the TENG sensor array in identifying adhesion strength of soft materials, six samples with different adhesion strengths (range from approximately 1.5 to 7.5 kPa) were selected for testing were tested using a linear motor-controlled setup (Figure 4a). Each material underwent a series of contact−separation cycles with the four-channel TENG sensor array (see Figure S10 for details). The acquired signals were then processed through feature extraction, followed by classification using a LDA model.

The classification results confirmed the sensor's ability to effectively distinguish between different adhesion strength, achieving an overall accuracy of approximately 96% (Figure 4b, Figure S6). Moreover, consistent with the trends observed in the modulus classification experiment, the number of sensor channels significantly impacted the identification performance for adhesion properties. As shown in Figure 4c, the integration of four sensing channels enabled high classification accuracy with relatively few repeated measurements. In contrast, reducing the number of channels limited performance improvements even with extensive repetitions, indicating that multichannel signal combination plays a critical role in improving the identification accuracy of adhesive properties.

Figure 4d provides a two-dimensional visualization of the classification results under different channels. The progression from single to four-channel reveals increasingly distinct clustering and clearer boundaries between material classes, further illustrating the advantage of multichannel combination in improving class separability for adhesive materials.

In summary, the experiments on modulus and adhesion strength identification demonstrate that the TENG sensor array exhibits strong sensitivity to various mechanical properties of soft materials. The integration of multichannel signals enables simultaneous differentiation of modulus and surface adhesion attributes, establishing a solid foundation for the subsequent multimodal data combination of triboelectric and piezoelectric signals.

2.4. Multimodal Measurement Results. To further evaluate the capability of the MSF in multidimensional identification of soft materials under practical conditions, we extended the experimental targets to 23 types of soft materials exhibiting diverse combinations of moduli and adhesion strengths (Figure 5a, Figure S7). LDA was employed to maximize interclass distances and minimize intraclass variability in a lower-dimensional space, facilitating effective classification. This method not only achieves positive classification accuracy but also provides interpretable feature weights and decision boundaries, making it well-suited for practical engineering applications. The raw signals were preprocessed and normalized, followed by a feature engineering stage involving multidimensional feature extraction. Redundant features were removed through feature selection techniques, retaining only those with significant contribution to the classification task. The refined high-quality feature matrix was then input into the LDA model for training and testing (Figure 5b).

https://doi.org/10.1021/acsami.5c17508
ACS Appl. Mater. Interfaces XXXX, XXX, XXX−XXX

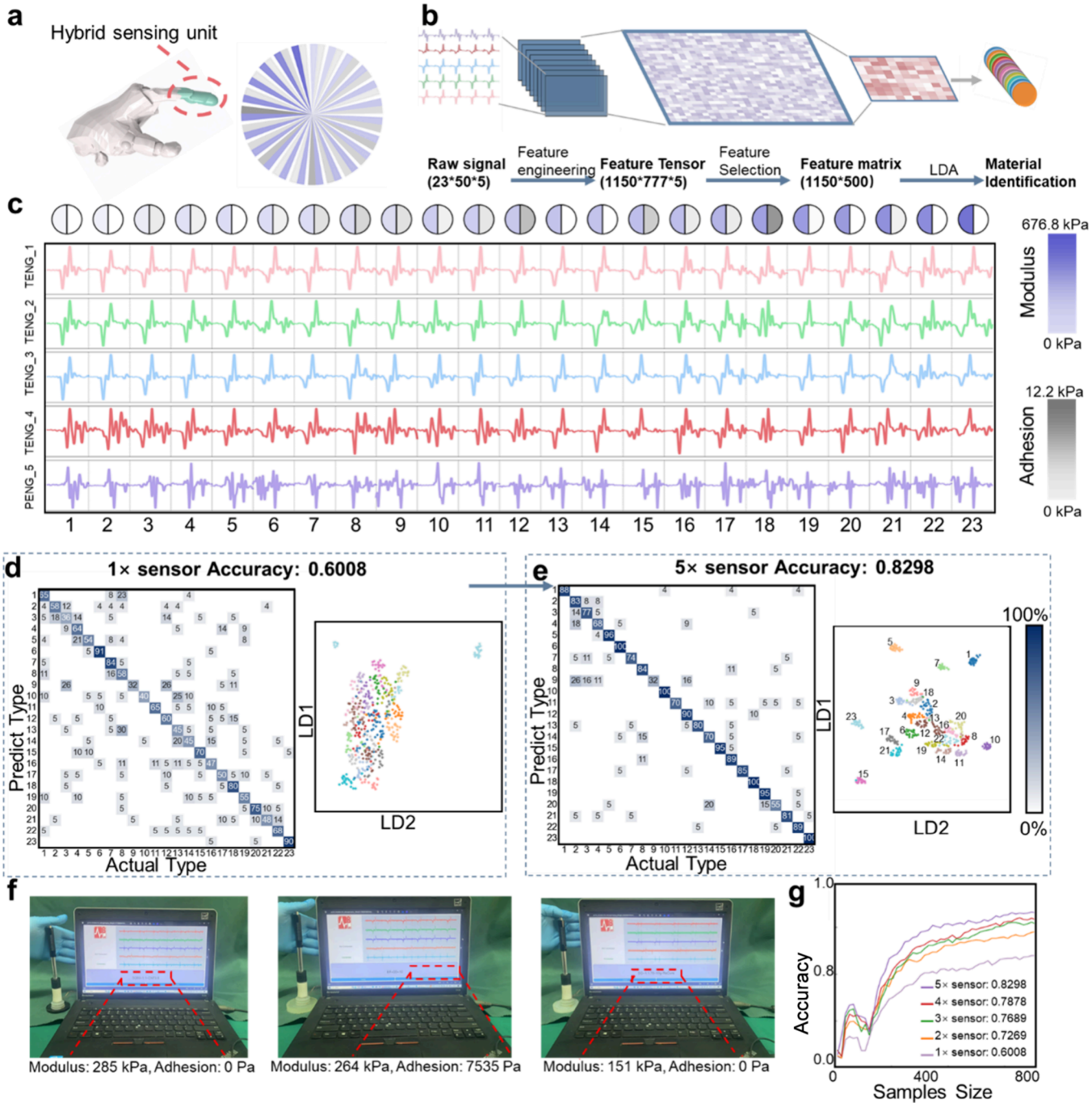

Figure 5. Practical application scenarios and identification performance. (a) Illustration of the smart finger measuring 23 soft materials with different combinations of modulus and adhesion strength. (b) Workflow for feature extraction and classification. (c) Representative five-channel sensing responses for 23 materials. (d-e) Comparison of LDA classification results using single-channel and five-channel signals, including confusion matrices and two-dimensional clustering. (f) Experimental photographs showing the smart finger operating on different materials. (g) Evolution of identification accuracy with training sample size across different sensor channel configurations.

During actual measurements (Figure 5f), the smart finger simultaneously acquired fourchannel triboelectric signals and one-channel piezoelectric signal, which represent the mechanical response of each material under contact conditions (Figure 5c).

Figures 5d and 5e compare the classification results between a single-channel input and the full five-channel Combination (four TENGs and one PENG). With only a single channel (PENG), the overall classification accuracy was approximately 60.1%, and the clustering of different materials in feature space exhibited substantial overlap and poor separability. In contrast, the combination of all five channels led to a markedly improved classification accuracy of approximately 83%, along with more distinct and well-defined cluster boundaries in the feature space (Figure S8). The individual classification accuracies of each sensing channel are provided in Supplementary Figure S12.

As the number of training samples increased (Figure 5g), the classification accuracy of models based on different sensor channel combinations consistently improved. Notably, models

https://doi.org/10.1021/acsami.5c17508
ACS Appl. Mater. Interfaces XXXX, XXX, XXX−XXX

incorporating more channels achieved higher accuracy more rapidly and exhibited more stable performance as sample size grew. These findings underscore the generalization capability of machine learning models when supplied with comprehensive feature information, significantly enhancing the reliability and applicability of the smart finger in real-world scenarios.

In conclusion, by employing a robust machine learning strategy that includes optimized feature extraction and integrated analysis, the challenges of high-dimensional information identification in complex material systems are effectively addressed. The developed MSF not only enables rapid and accurate identification of the multidimensional mechanical properties of soft materials, but also offers a versatile and efficient data analysis framework applicable to sensor design and soft material evaluation in future applications.

CONCLUSION

In this study, we developed an MSF based on the synergistic integration of TENG and PENG, enabling rapid identification of soft materials. Our work extends the applicability of TENG sensors to the identification of soft materials. In contrast to conventional techniques, the proposed method significantly reduces measurement costs, enhances operational simplicity and efficiency, and offers advantages in real-time response and portable deployment. The integration of a self-locking structural module significantly contributes to the improvement of recognition accuracy in the multimodal sensing system, as it ensures consistent mechanical coupling during repeated contact events. This structural design enhances the repeatability and consistency of the measurement process, enabling stable data acquisition without the need for precision loading equipment. In actual testing, the system utilized five-channel sensor inputs to achieve an identification accuracy exceeding 83% across 23 soft materials with a wide range of moduli and adhesion strengths, demonstrating that multimodal sensor combination significantly improves material discriminability.

The current results demonstrate that the proposed system combines structural simplicity, rapid response, and rich signal information to effectively support soft material identification. Although the synergistic advantages of TENG and PENG in soft material recognition are confirmed, certain general limitations remain, such as the need for improved robustness under diverse operating conditions and broader applicability across more complex material scenarios. Future work may involve the integration of additional sensory modalities (e.g., pressure, temperature) and the deployment of more advanced machine learning algorithms, as well as a systematic exploration of alternative triboelectric materials with diverse chemical compositions and surface energy characteristics. The development process may also reference open-source hardware and software frameworks (see Figure S13) to support system-level integration. These efforts will further broaden the applicability of such intelligent sensors in medical rehabilitation, soft robotics, and material characterization.

EXPERIMENTAL SECTION

For clarity, the main machine-learning terminologies and workflow used in this study are briefly defined in the Supporting Information (Section S1).

Fabrication of the Smart Finger. The TENG sensor array consists of four TENG units. The substrate was prepared by mixing Sylgard 184 PDMS elastomer and curing agent in a mass ratio of 10:1, followed by casting the mixture into a sector mold (1 cm radius) and curing at 40 °C. After curing, a conductive metal layer was deposited on the substrate surface, and conductive wires were fixed to form electrodes. The four TENG units were prepared using different soft friction layer materials: PDMS elastomers with two mixing ratios (10:1 and 20:1), liquid silica gel (POSILICONE), and Ecoflex silicone rubber. The uncured mixtures were poured into the respective cavities of the array substrate, allowed to level naturally, and then cured at 40 °C to obtain the complete TENG sensor array.

The PENG sensor module was constructed using a 50 μm-thick PVDF film (6 mm × 10 mm), with one end fixed to a 3D-printed supporting structure and the free end attached to a small mass block to increase vibration inertia. The metal electrodes on the PVDF surface were connected to external leads through a through-contact structure to ensure stable signal extraction. A copper guiding structure was placed at the center of the TENG sensor array to constrain the impact axis along the axial direction and minimize lateral deviations. The entire sensing structure was assembled with a commercial housing and suction cup component to form a complete multimodal sensing probe. The supporting framework was fabricated using custom 3D-printed parts, while the guiding system consisted of customized metal rails and an impact rod. The dimensions and geometry of these components were simplified to meet both functional and assembly requirements(Figure S14). The triboelectric structure consists of a friction layer, conductive coating, electrode wiring, and flexible substrate, with corresponding thicknesses of approximately 1.0 mm and 0.2 mm for the friction and conductive layers, respectively. Each triboelectric unit was connected to the oscilloscope positive terminal via a conductive wire, while the negative terminal was grounded. For the piezoelectric module, the PVDF film (commercial, 52 μm thick, purchased from PolyK Technologie) was poled and has a nominal d_{33} of 25−32 pC/N, as specified by the manufacturer.

Characterization and Measurements. All measurements were performed under controlled laboratory conditions (25 °C, 35% RH). A linear motor (model E1100, LinMot) was used to generate periodic contact−release motions with a descending velocity of 10 mm s^{-1}. A force sensor positioned beneath the sample continuously monitored contact force, maintaining a load of 2 ± 0.1 N during each test. The valid sample numbers for each experimental test are summarized in Supplementary Figure S10. The output performance of all sensors was measured using an oscilloscope. Triboelectric measurements were performed using a linear motor to simulate controlled contact−separation cycles. During testing, the negative electrode of the sensor circuit was grounded to minimize external electromagnetic interference.

Signal Processing Workflow. In this study, both triboelectric and piezoelectric signals were processed through a unified signal segmentation and screening procedure. Each data set was divided into contact−release windows based on peak detection, and the corresponding baseline noise level was used to exclude segments with insufficient signal quality.

The segmented raw signals were then directly used for feature extraction without additional filtering or baseline correction, so as to preserve their intrinsic waveform morphology. Multidimensional features were computed using the extract_features function from the tsfresh Python library with the EfficientFCParameters configuration, which provides a comprehensive framework for time-series feature extraction. The extracted descriptors covered both time- and frequency-domain characteristics, including statistical parameters (mean, variance, skewness, kurtosis), amplitude-related indices (peak value, energy), and spectral-domain features (dominant frequency components and spectral energy).

For the subsequent classification, the mechanical parameters of the tested materials (elastic modulus and viscosity) were normalized to comparable scales to prevent bias arising from magnitude differences. The resulting feature matrix, together with the normalized material parameters, was divided into training and validation sets and used as input to a Linear Discriminant Analysis (LDA) classifier to identify the optimal feature combinations for material discrimination. For

https://doi.org/10.1021/acsami.5c17508
ACS Appl. Mater. Interfaces XXXX, XXX, XXX−XXX

clarity, the main machine-learning terminologies and workflow used in this study are briefly defined in the Supporting Information (Section S1).

Mechanical Characterization of Test Samples. The elastic modulus and surface adhesion strength of each test sample were measured using a MARE-10 mechanical testing system (Figure S9). A flat-ended probe with a contact area of 1 cm^2 was pressed vertically into the material surface at a constant speed to obtain the force−displacement curve. After reaching a predefined indentation depth, the probe was retracted at the same speed. For samples exhibiting adhesive behavior, a distinct pull-off force was observed during separation. Both the elastic modulus and adhesion strength were calculated from the recorded force curve and known contact area. The test samples were fabricated from PDMS, Ecoflex, and commercial silicone rubbers. The mixtures were poured into molds at various volumes and cured at 40 °C to obtain elastomers with a broad range of mechanical properties.

■ ASSOCIATED CONTENT

Supporting Information

The Supporting Information is available free of charge at https://pubs.acs.org/doi/10.1021/acsami.5c17508.

Supplementary figures (Figure S1−S16) including supplementary experimental/characterization data and device/circuit details, supplementary table summarizing current material identification technologies (Table S1), and terminology clarification for machine-learning analysis (Section S1) (PDF)

■ AUTHOR INFORMATION

Corresponding Authors

Puchuan Tan − *Beijing Institute of Nanoenergy and Nanosystems, Chinese Academy of Sciences, Beijing 101400, China*; Email: tanpuchuan@ucas.ac.cn

Zhou Li − *School of Physical Science and Technology, Guangxi University, Nanning 530004, China; Vita Tech Innovation Center, Beijing Tsinghua Changgung Hospital, School of Clinical Medicine, Tsinghua University, Beijing 102218, China; School of Biomedical Engineering, Tsinghua University, Beijing 100084, China;* orcid.org/0000-0002-9952-7296; Email: li_zhou@tsinghua.edu.cn

Authors

Lu Wang − *School of Physical Science and Technology, Guangxi University, Nanning 530004, China; Beijing Institute of Nanoenergy and Nanosystems, Chinese Academy of Sciences, Beijing 101400, China*

Xuecheng Qu − *Vita Tech Innovation Center, Beijing Tsinghua Changgung Hospital, School of Clinical Medicine, Tsinghua University, Beijing 102218, China*

Shengyu Chao − *Beijing Institute of Nanoenergy and Nanosystems, Chinese Academy of Sciences, Beijing 101400, China*

Yuan Xi − *Beijing Institute of Nanoenergy and Nanosystems, Chinese Academy of Sciences, Beijing 101400, China; Key Laboratory of Biomechanics and Mechanobiology of Ministry of Education Advanced Innovation Center for Biomedical Engineering School of Engineering Medicine, Beihang University, Beijing 100191, China*

Yang Zou − *Vita Tech Innovation Center, Beijing Tsinghua Changgung Hospital, School of Clinical Medicine, Tsinghua University, Beijing 102218, China;* orcid.org/0000-0003-2557-4230

Cong Li − *Beijing Institute of Nanoenergy and Nanosystems, Chinese Academy of Sciences, Beijing 101400, China; Institute of Chinese Materia Medica China Academy of Chinese Medical Sciences, Beijing 100700, China*

Jiangtao Xue − *Beijing Institute of Nanoenergy and Nanosystems, Chinese Academy of Sciences, Beijing 101400, China; School of Medical Technology, Beijing Institute of Technology, Beijing 100081, China*

Complete contact information is available at: https://pubs.acs.org/10.1021/acsami.5c17508

Author Contributions

§L.W., P.T., and X.Q. contributed equally to this work.

Notes

The authors declare no competing financial interest.

■ ACKNOWLEDGMENTS

This work was supported by the National Key Research and Development Program of China (2022YFB3804700), the Natural Science Foundation of Beijing Municipality (L245015), China Postdoctoral Science Foundation (2023M743446), National Natural Science Foundation of China (T2125003, 52405320), and the Fundamental Research Funds for the Central Universities.

■ REFERENCES

(1) Deflorio, D.; Di Luca, M.; Wing, A. M. Skin and Mechanoreceptor Contribution to Tactile Input for Perception: A Review of Simulation Models. *Front Hum Neurosci* **2022**, *16*, No. 862344.

(2) Amoli, V.; Kim, J. S.; Kim, S. Y.; Koo, J.; Chung, Y. S.; Choi, H.; Kim, D. H. Ionic Tactile Sensors for Emerging Human-Interactive Technologies: A Review of Recent Progress. *Adv. Funct. Mater.* **2020**, *30* (20), No. 1904532.

(3) Basdogan, C.; Giraud, F.; Levesque, V.; Choi, S. A Review of Surface Haptics: Enabling Tactile Effects on Touch Surfaces. *IEEE Trans Haptics* **2020**, *13* (3), 450−470.

(4) Corniani, G.; Saal, H. P. Tactile innervation densities across the whole body. *J. Neurophysiol* **2020**, *124* (4), 1229−1240.

(5) Wang, H.; Totaro, M.; Beccai, L. Toward Perceptive Soft Robots: Progress and Challenges. *Adv. Sci. (Weinh)* **2018**, *5* (9), No. 1800541.

(6) Li, Q.; Kroemer, O.; Su, Z.; Veiga, F. F.; Kaboli, M.; Ritter, H. J. A Review of Tactile Information: Perception and Action Through Touch. *IEEE Transactions on Robotics* **2020**, *36* (6), 1619−1634.

(7) Shang, Y.; Huang, C.; Li, Z.; Du, X. Bioinspired Ultra-Stretchable and Highly Sensitive Structural Color Electronic Skins. *Adv. Funct. Mater.* **2025**, *35* (2), No. 2412703.

(8) Liu, Y.; Wang, C.; Xue, J.; Huang, G.; Zheng, S.; Zhao, K.; Huang, J.; Wang, Y.; Zhang, Y.; Yin, T.; et al. Body Temperature Enhanced Adhesive, Antibacterial, and Recyclable Ionic Hydrogel for Epidermal Electrophysiological Monitoring. *Adv. Healthc Mater.* **2022**, *11* (15), No. e2200653.

(9) Li, C.; Luo, Z.; Feng, H.; Li, Z. Polymers Facilitating Therapeutic Efficacy and Applications for Traditional Chinese Medicine. *J. Polym. Sci.* **2025**, *63* (4), 839−863.

(10) Ambrosi, D.; Ben Amar, M.; Cyron, C. J.; DeSimone, A.; Goriely, A.; Humphrey, J. D.; Kuhl, E. Growth and remodelling of living tissues: perspectives, challenges and opportunities. *J. R Soc. Interface* **2019**, *16* (157), No. 20190233.

(11) Yang, J. C.; Mun, J.; Kwon, S. Y.; Park, S.; Bao, Z.; Park, S. Electronic Skin: Recent Progress and Future Prospects for Skin-Attachable Devices for Health Monitoring, Robotics, and Prosthetics. *Adv. Mater.* **2019**, *31* (48), No. e1904765.

(12) Chen, C.; Hu, Z.; Liu, S.; Tseng, H. Emerging trends in regenerative medicine: a scientometric analysis in CiteSpace. *Expert Opin Biol. Ther* **2012**, *12* (5), 593−608.
(13) Zeng, X.; Teng, L.; Wang, X.; Lu, T.; Leng, W.; Wu, X.; Li, D.; Zhong, Y.; Sun, X.; Zhu, S.; et al. Efficient multi-physical crosslinked nanocomposite hydrogel for a conformal strain and self-powered tactile sensor. *Nano Energy* **2025**, *135*, No. 110669.
(14) Miller, H.; Zhou, Z.; Shepherd, J.; Wollman, A. J. M.; Leake, M. C. Single-molecule techniques in biophysics: a review of the progress in methods and applications. *Rep. Prog. Phys.* **2018**, *81* (2), No. 024601.
(15) Rubiano, A.; Galitz, C.; Simmons, C. S. Mechanical Characterization by Mesoscale Indentation: Advantages and Pitfalls for Tissue and Scaffolds. *Tissue Eng. Part C Methods* **2019**, *25* (10), 619−629.
(16) Yuan, S.; Tian, Y.; Li, Y.; Li, S.; Fu, L.; Li, T.; Zhang, T. A selectively bimodal flexible sensor based on IL/SWCNTs/PEDOT:PSS nanocomposites for materials and shape recognition. *Journal of Materials Chemistry C* **2024**, *12* (10), 3611−3621.
(17) Zhu, B.; Geng, T.; Jiang, G.; Guan, Z.; Li, Y.; Yun, X. Surrounding Object Material Detection and Identification Method for Robots Based on Ultrasonic Echo Signals. *Appl. Bionics Biomech.* **2023**, *2023*, No. 1998218.
(18) Shi, Y.; Ong, H. R.; Yang, S.; Fan, Y. Deep Multimodal Fusion of Visual and Auditory Features for Robust Material Recognition. *Int. J. Comput. Commun. Control* **2024**, *19* (5). DOI:.
(19) Dhahri, A.; Amamou, A.; Faghihi, U.; Kelouwani, S.; Boisclair, J.; Zeghmi, L. Surface multi-spectral reflectivity and texture material recognition in non-constrained environments. *Mach. Vision Appl.* **2025**, *36* (5), 99.
(20) Wu, E.; Liang, J.; Kim, N.; Jang, Y.; Kim, E.; Yan, M.; Wu, J.; Wang, C.; Gu, X.; Li, Y. Wireless Passive Flexible Radio Frequency Tactile Sensor for Material Recognition. *Nano Lett.* **2025**, *25* (19), 7960−7968.
(21) Hu, S.; Wang, R.; Zhu, W.; Huang, Y.; Li, Y.; Yang, Y.; Zhang, Q.; Yan, Y.; Lin, C.; Deng, Y. Sub-millimeter scale 3D integration strategy enables ultrahigh-density and ultralow-crosstalk flexible tactile sensor array for robotic e-skin application. *Chem. Eng. J.* **2024**, *502*, No. 157950.
(22) Cao, V. A.; Phan, V. Q.; Nguyen, N. K.; Kim, M.; Van, P. C.; Minh, H. N.; Kim, S. Y.; Nah, J. Multifunctional tactile sensor with multimodal capabilities for pressure, temperature, and surface recognition. *Nano Energy* **2025**, *136*, No. 110706.
(23) Man, J.; Jin, Z.; Chen, J. Magnetic Tactile Sensor with Bionic Hair Array for Sliding Sensing and Object Recognition. *Adv. Sci. (Weinh)* **2024**, *11* (12), No. e2306832.
(24) Zacharia, V.; Bardakas, A.; Anastasopoulos, A.; Moustaka, M. A.; Hourdakis, E.; Tsamis, C. Design of a flexible tactile sensor for material and texture identification utilizing both contact-separation and surface sliding modes for real-life touch simulation. *Nano Energy* **2024**, *127*, No. 109702.
(25) Qian, M.; Dong, Y.; Wang, W.; Li, D.; Sun, T.; Zhang, Q. Hardness recognition using a fiber Bragg grating flexible tactile sensor. *Opt. Laser Technol.* **2025**, *192*, No. 113714.
(26) Kim, W. G.; Kim, D. W.; Tcho, I. W.; Kim, J. K.; Kim, M. S.; Choi, Y. K. Triboelectric Nanogenerator: Structure, Mechanism, and Applications. *ACS Nano* **2021**, *15* (1), 258−287.
(27) Zhao, G.; Zhang, Y.; Shi, N.; Liu, Z.; Zhang, X.; Wu, M.; Pan, C.; Liu, H.; Li, L.; Wang, Z. L. Transparent and stretchable triboelectric nanogenerator for self-powered tactile sensing. *Nano Energy* **2019**, *59*, 302−310.
(28) Zhang, Z.; Liu, G.; Li, Z.; Zhang, W.; Meng, Q. Flexible tactile sensors with biomimetic microstructures: Mechanisms, fabrication, and applications. *Adv. Colloid Interface Sci.* **2023**, *320*, No. 102988.
(29) Pyo, S.; Lee, J.; Bae, K.; Sim, S.; Kim, J. Recent Progress in Flexible Tactile Sensors for Human-Interactive Systems: From Sensors to Advanced Applications. *Adv. Mater.* **2021**, *33* (47), No. e2005902.
(30) Meena, K. K.; Arief, I.; Ghosh, A. K.; Liebscher, H.; Hait, S.; Nagel, J.; Heinrich, G.; Fery, A.; Das, A. 3D-printed stretchable hybrid piezoelectric-triboelectric nanogenerator for smart tire: Onboard real-time tread wear monitoring system. *Nano Energy* **2023**, *115*, No. 108707.
(31) Meena, K. K.; Arief, I.; Ghosh, A. K.; Knapp, A.; Nitschke, M.; Fery, A.; Das, A. Transfer-Printed Wrinkled PVDF-Based Tactile Sensor-Nanogenerator Bundle for Hybrid Piezoelectric-Triboelectric Potential Generation. *Small* **2025**, *21* (26), No. e2502767.
(32) Wu, C.; Wang, A. C.; Ding, W.; Guo, H.; Wang, Z. L. Triboelectric Nanogenerator: A Foundation of the Energy for the New Era. *Adv. Energy Mater.* **2019**, *9* (1), No. 1802906.
(33) Wang, Z. L.; Wang, A. C. On the origin of contact-electrification. *Mater. Today* **2019**, *30*, 34−51.
(34) Wang, Z. L. From contact electrification to triboelectric nanogenerators. *Rep. Prog. Phys.* **2021**, *84* (9), No. 096502.
(35) Zhang, W.; Xi, Y.; Wang, E.; Qu, X.; Yang, Y.; Fan, Y.; Shi, B.; Li, Z. Self-Powered Force Sensors for Multidimensional Tactile Sensing. *ACS Appl. Mater. Interfaces* **2022**, *14* (17), 20122−20131.
(36) Wang, Y.; Tan, P.; Wu, Y.; Luo, D.; Li, Z. Artificial intelligence-enhanced skin-like sensors based on flexible nanogenerators. *VIEW* **2022**, *3* (5), No. 20220026.
(37) Qu, X.; Liu, Z.; Tan, P.; Wang, C.; Liu, Y.; Feng, H.; Luo, D.; Li, Z.; Wang, Z. L. Artificial tactile perception smart finger for material identification based on triboelectric sensing. *Sci. Adv.* **2022**, *8* (31), No. eabq2521.
(38) Yang, W.; Wang, X.; Chen, P.; Hu, Y.; Li, L.; Sun, Z. On the controlled adhesive contact and electrical performance of vertical contact-separation mode triboelectric nanogenerators with micro-grooved surfaces. *Nano Energy* **2021**, *85*, No. 106037.
(39) Verners, O.; Šutka, A.; Arief, I.; Das, A.; Mālnieks, K.; Lungevičs, J. The effect of surface texture components on the contact electrification of triboelectric materials: A theoretical study. *Mater. Sci. Eng.: B* **2025**, *317*, No. 118140.
(40) Cao, Y.; Cao, W.; Yang, X.; Liu, C.; Qi, X. Theoretical investigation of polymer molecular structure influence on dielectric properties and mechanical properties. *Polymers for Advanced Techs* **2022**, *33* (1), 146−153.
(41) Yang, W.; Wang, X.; Li, H.; Wu, J.; Hu, Y. Comprehensive contact analysis for vertical-contact-mode triboelectric nanogenerators with micro-/nano-textured surfaces. *Nano Energy* **2018**, *51*, 241−249.
(42) Hu, Y.; Wang, X.; Li, H.; Li, H.; Li, Z. Effect of humidity on tribological properties and electrification performance of sliding-mode triboelectric nanogenerator. *Nano Energy* **2020**, *71*, No. 104640.
(43) Guan, D.; Cong, X.; Li, J.; Shen, H.; Zhang, C.; Gong, J. Quantitative characterization of the energy harvesting performance of soft-contact sphere triboelectric nanogenerator. *Nano Energy* **2021**, *87*, No. 106186.
(44) Li, J.; Shepelin, N. A.; Sherrell, P. C.; Ellis, A. V. Poly(dimethylsiloxane) for Triboelectricity: From Mechanisms to Practical Strategies. *Chem. Mater.* **2021**, *33* (12), 4304−4327.
(45) Yang, D.; Guo, H.; Chen, X.; Wang, L.; Jiang, P.; Zhang, W.; Zhang, L.; Wang, Z. L. A flexible and wide pressure range triboelectric sensor array for real-time pressure detection and distribution mapping. *J. Mater. Chem. A* **2020**, *8* (45), 23827−23833.
(46) Sezer, N.; Koç, M. A comprehensive review on the state-of-the-art of piezoelectric energy harvesting. *Nano Energy* **2021**, *80*, No. 105567.
(47) Sarker, M. R.; Julai, S.; Sabri, M. F. M.; Said, S. M.; Islam, M. M.; Tahir, M. Review of piezoelectric energy harvesting system and application of optimization techniques to enhance the performance of the harvesting system. *Sensors and Actuators A: Physical* **2019**, *300*, No. 111634.
(48) Liu, H.; Zhong, J.; Lee, C.; Lee, S.-W.; Lin, L. A comprehensive review on piezoelectric energy harvesting technology: Materials, mechanisms, and applications. *Applied Physics Reviews* **2018**, *5* (4), No. 041306.
(49) Izadgoshasb, I.; Lim, Y. Y.; Tang, L.; Padilla, R. V.; Tang, Z. S.; Sedighi, M. Improving efficiency of piezoelectric based energy

https://doi.org/10.1021/acsami.5c17508
ACS Appl. Mater. Interfaces XXXX, XXX, XXX−XXX

harvesting from human motions using double pendulum system. *Energy Conversion and Management* **2019**, *184*, 559−570.
(50) Ju, S.; Ji, C.-H. Impact-based piezoelectric vibration energy harvester. *Applied Energy* **2018**, *214*, 139−151.
(51) Fan, K.; Tan, Q.; Zhang, Y.; Liu, S.; Cai, M.; Zhu, Y. A monostable piezoelectric energy harvester for broadband low-level excitations. *Appl. Phys. Lett.* **2018**, *112* (12), No. 123901.
(52) Fan, H.; Tan, P.; Bai, Y.; Xi, Y.; Wang, E.; Yin, M.; Wen, X.; Li, T.; Xue, J.; Zou, Y.; et al. The triboelectric performance of natural friction materials from traditional Chinese herbs repository. *Nano Energy* **2025**, *141*, No. 111088.
(53) Wu, Y.; Li, Y.; Zou, Y.; Rao, W.; Gai, Y.; Xue, J.; Wu, L.; Qu, X.; Liu, Y.; Xu, G.; et al. A multi-mode triboelectric nanogenerator for energy harvesting and biomedical monitoring. *Nano Energy* **2022**, *92*, No. 106715.
(54) Kong, F.; Zou, Y.; Li, Z.; Deng, Y. Advances in Portable and Wearable Acoustic Sensing Devices for Human Health Monitoring. *Sensors* **2024**, *24* (16), 5354.

https://doi.org/10.1021/acsami.5c17508
ACS Appl. Mater. Interfaces XXXX, XXX, XXX−XXX